
Article:
Atwya, M., Kavak, C., Alisse, E. et al. (2 more authors) (2021) Flexible and expandable robot for tissue therapies - Modeling and design. IEEE Transactions on Biomedical Engineering, 68 (2). pp. 568-578. ISSN 0018-9294

https://doi.org/10.1109/TBME.2020.3007714

Flexible and Expandable Robot for Tissue Therapies - Modeling and Design

Mohamed Atwya[1], Can Kavak[2], Elodie Alisse[3], YanQiang Liu[4], and Dana D. Damian[1]

***Abstract*—Objective: Implantable technologies should be mechanically compliant with the tissue in order to maximize tissue quality and reduce inflammation during tissue reconstruction. We introduce the development of a flexible and expandable implantable robotic (FEIR) device for the regenerative elongation of tubular tissue by applying controlled and precise tension to the target tissue while minimizing the forces produced on the surrounding tissue. Methods: We introduce a theoretical framework based on iterative beam theory static analysis for the design of an expandable robot with a flexible rack. The model takes into account the geometry and mechanics of the rack to determine a trade-off between its stiffness and capability to deliver the required tissue tension force. We empirically validate this theory on the benchtop and with biological tissue. Results: We show that FEIR can apply the required therapeutical forces on the tissue while reducing the amount of force it applies to the surrounding tissues as well as reducing self-damage. Conclusion: The study demonstrates a method to develop robots that can change size and shape to fit their dynamic environment while maintaining the precision and delicacy necessary to manipulate tissue by traction. Significance: The method is relevant to designers of implantable technologies. The robot is a precursor medical device for the treatment of Long-Gap Esophageal Atresia and Short Bowel Syndrome.**

***Index Terms*—Flexible robot, expandable robot, robotic implants**

NOMENCLATURE

F_{1r},F_{1x}	Worm screw radial and axial force components, respectively.
F_{2t},F_{2r}	Rack tangential and radial force components.
F_{3x},F_{3sk}	Axial force acting on the rail and Static/kinetic friction force between the rack and rail.
R_{3y}	Vertical reaction force of the rail on the rack.
F_{4x}	Desired tension force in the esophagus.
M_0,M_1	Bending moment acting on the rack as result of force F_{4x} and the reaction moment.
R_{5x},R_{5r}	Horizontal and vertical reaction forces of the fixed support on the rack.
R_{5e}	Reaction force of the fixed support on the esophagus.
T	DC gearmotor torque.
S_f	DC gearmotor torque safety factor.
μ_{sw},μ_{sr}	Static worm/rack and static rack/rail dry friction coefficients.
d_1	Reference diameter of the worm screw.
α_n,γ	Normal pressure angle and the reference cylinder lead angle of the worm screw.
η_r	Efficiency of the worm screw and rack gear configuration.

[1] M. Atwya and D.D. Damian are with the University of Sheffield, UK (e-mail: d.damian@sheffield.ac.uk). [2] C. Kavak is with the Izmir Institute of Technology, Turkey. [3] E. Alisse is with ESEO, France. [4] Y. Liu is with Beihang University, China.

This work was supported by The University of Sheffield, EPSRC grants #R/150439 and #EP/S021035/1.

I. INTRODUCTION

TISSUE healing and regeneration are lengthy and physiologically demanding processes that do not always follow a smooth physiological path (i.e., healing); undesired pathologies can also develop, from simpler forms like tissue strictures to complex ones like neoplasms [1]. It is not uncommon for these postoperative complications to require follow-up medical procedures and even surgery.

For such cases, long-term treatment is required and this entails a need of sustainable medical assistance.For instance, long-gap esophageal atresia (LGEA) is a congenital defect in which a section of the esophagus, 3 mm or more in length, is missing. Currently, the most popular LGEA treatment , the Foker technique, consists of attaching sutures to the end of the esophageal stubs, looping them around the ribs, and tying them off at the child's back. The sutures are then tightened for weeks to encourage tissue to elongate, after which the gap is closed by surgery. During treatment, the baby needs to be sedated, and frequent X-rays is required to monitor tissue elongation [2].

To avoid cases of morbidity in this otherwise successful treatment, it would be ideal to have a robotic implant that resides inside the body, mounted on the esophageal stub. This implant could mimic the Foker technique until the tubular organ is fully reconstructed. Implantable technologies that can operate in the long term inside the body and provide on board clinical feedback until the tissue heals can facilitate long-term therapies. Such robotic implantable devices not only could complement a surgeon's capabilities but could also provide specific actions and assessments that are usually not available to surgeons, such as assessments of tissue mechanical properties, which are important cues to evaluate healing. These devices can deliver effective therapy at all times during treatment through their ability to operate autonomously [3], which is impossible in typical forms of clinical practice. Robotic implantable technology also has the potential to adjust and customize treatments, depending on the target tissue and patient state. Lastly, treatment costs can be dramatically reduced, as part of the treatment can be carried out at home.

While robotic implantable devices can bring significant treatment outcomes, clinical challenges associated with their long-term use do exist. Foreign bodies, including any im-

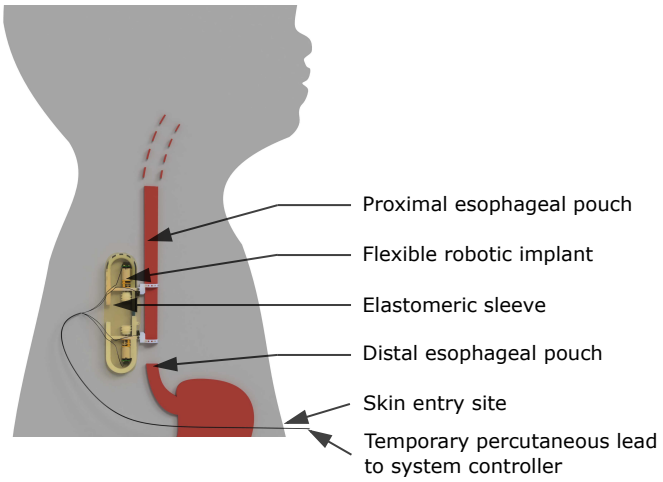
Proximal esophageal pouch
Flexible robotic implant
Elastomeric sleeve
Distal esophageal pouch
Skin entry site
Temporary percutaneous lead
to system controller

III. Implant Requirements and Design

A. Requirements

Our in vivo studies [17] have revealed unrecognized challenges owing to the fixed design of the implant operating over the long term in a harsh in vivo environment.

a) Implant flexibility: the robotic implant must be mechanically compliant (flexible) with the surrounding soft tissue. We have ascertained in our previous work that tissue fibrosis occurred at a notable level due to the contact forces between the rigid implant and tissue [17]. A flexible robotic implant should inflict less damage to the surrounding organs and minimize fibrotic response [4]. The flexibility feature is even more essential for an implant that operates in the chest cavity, where the organs are vital and tightly packed, and there are considerable dynamics due to lung inflation and heartbeat. In addition, the flexibility of the implant should help maintain the integrity of the elastomeric encapsulation of the robotic implant [17]. Because the robot is near the ribs, the ribs are prone to cause the encapsulation to deteriorate over time due to the shear stress exerted on the elastomeric encapsulation.

b) Tension force in tissue: based on our previous work, the robotic implant must be capable of applying a tension force to the tissue of up to $2.00\,\mathrm{N}$.

c) Tissue elongation: the robot needs to provide approximately $100.00\,\mathrm{mm}$ tissue displacement capability, which is sufficient for LGEA [18], [19].

d) Fault-tolerance: the robotic implant should also be resilient to fault in order to guarantee its long-term use, which can range from weeks to months of treatment.

In this study, we aim to address the first three of these challenges.

B. Implant Design

Based on the above design requirements, we advance our robotic implant [17] with a flexible rack. The FEIR consists of four modules: two identical rail assemblies, a flexible rack, and an encapsulation sleeve as shown in Fig. 1 and Fig. 2. Each rail houses a DC gearmotor with an encoder, a worm screw, a force sensor, and a ring for tissue attachment. The implant design features identical rails which provide redundant mechanisms to facilitate redundancy-based fault-tolerance (this topic is beyond the scope of this study). The electronic design is presented in Section IX-A of the Supplementary Material.

The implant attaches to a tubular tissue using two attachment rings through sutures. The bidirectional DC gearmotor and worm screw configuration allow the rails to move across the flexible rack, increasing the distance between the two rings and applying tension to the tissue. The tension and elongation are monitored via the force sensor and encoder, respectively. The implant is encapsulated in a biomedical-grade elastomeric sleeve to shield the electrical components [17] (Fig. 2b). The encapsulation is wrinkled such that it does not apply a resistive force to FEIR as it expands to its maximum length (Fig. 3). In this study, the encapsulation is addressed through a proxy that is sufficient to test the effect of flexibility on its integrity. In the subsections below, we present the details of the FEIR design and development.

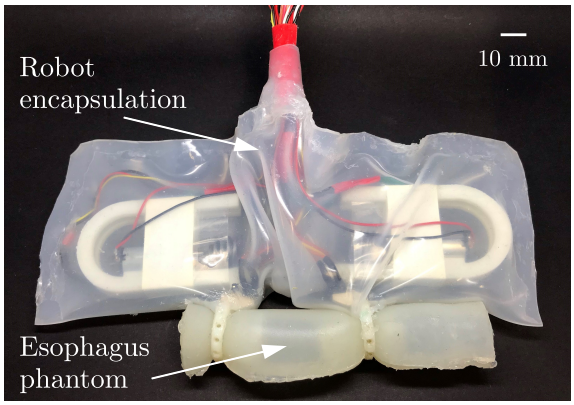

Fig. 3. Illustration of the FEIR and the proxy elastomeric encapsulation.

A flexible rack was used to ensure that the implant would comply with the dynamics of the surrounding tissue to avoid applying excessive stress to the organs in its proximity. The details of the rack are presented in Section V. Two identical U-shaped rails, also referred to as the main and mirror rails, guide the rack displacement. The U-shape of the rail enables housing an extra length of rack while reducing the overall length of the robotic implant.

The dimensions of the rail are as follows: height = $67.35\,\mathrm{mm}$, width = $38.51\,\mathrm{mm}$, and thickness = $15.30\,\mathrm{mm}$. The overall length of the robot is $135.00\,\mathrm{mm}$ (when the two rails are in contact), and the width is $35.00\,\mathrm{mm}$; these dimensions are $35.00\,\%$ and $16.00\,\%$ larger than their respective counterparts in [17]. The weight of the implant prototype is $45.00\,\mathrm{g}$. With this design, the maximum usable rack length and tissue elongation ranges between 23.00 and $230.00\,\mathrm{mm}$, depending on the rack's material and geometrical design parameters.

The tension force applied to the tissue by the implant is controlled via a proportional-integral (PI) controller. The FEIR and an elastomer esophagus phantom were modelled and simulated to aid in choosing the proportional and integral terms of the controller (see further details in Section IX-E of the Supplementary Material).

IV. Flexible Rack and Tissue Tension Modelling

Although flexibility is desired to ensure the implant's mechanical compliance with the target and surrounding tissues, the bending of the implant reduces the maximum tension force and tissue elongation length. Therefore, a trade-off between flexibility and the maximum tension force/elongation length is necessary to meet the clinical requirements of LGEA. We introduce a model based on an iterative beam theory static analysis to provide a theoretical framework for the choice and optimisation of the geometrical and mechanical properties of the rack in order to satisfy the clinical requirements.

We approximate the esophagus as an Ecoflex phantom with a tubular hollow shape. The silicone-made phantom only simulates the elastic deformation of the tissue, and not the tissue's growth (i.e. the phantom stretches but does not grow over time). Therefore, the phantom only simulates the esophagus from its resting state to its maximum elastically deformed state. In this study, modelling/simulation beyond the

elastic region assumes that as the phantom grows in length, the Young's modulus does not change. The esophagus phantom is characterized in Section IX-C of the Supplementary Material.

We approximate the maximum FEIR-induced tissue tension ($\overrightarrow{F_{4x}}$) via a non-linear hyper-elastic model of the esophagus phantom. The hyper-elastic model approximates the phantom as a Neo-Hookean solid to find the phantom tension ($\overrightarrow{F_{4x}}$) as a non-linear function of the phantom strain (Eq. 1). Note that the vector notation $\rightarrow$ will be omitted from the text for clarity.

As Fig. 4 shows, when the tissue is under tension, the tension F_{4x} applies a bending moment, M_0, on the rack. If the implant is rigid, then θ is constantly $0.00\,^\circ$ and the change in length of the rack (S) is equal to the change in length of the phantom $L_{p,crd}(0) = S$. However, when the implant is flexible, it bends as a function of the bending moment (M_0) which acts on the rack during expansion (Fig. 4). If the implant bends during the expansion period, the displacement between the two attachment rings (i.e., the tissue change in length) is less than the rack expansion length. In other words, the implant forms an arc with a certain arc length (S) and the tissue is elongated to the chord length ($L_{p,crd}$), where $L_{p,crd} < S$. Consequently, the maximum tissue tension (F_{4x}) also decreases as a function of the implant bend angle.

$$\overrightarrow{F_{4x}} = 2\frac{E_p}{6}A_p\big(\overrightarrow{\lambda} - \frac{1}{\overrightarrow{\lambda}\odot\overrightarrow{\lambda}}\big), \tag{1}$$

where E_p is the phantom's Young's modulus, A_p is the phantom's cross-section area perpendicular to the tension force, and λ is the natural strain (stretch).

$$\overrightarrow{\epsilon} = \frac{\overrightarrow{L_{p,crd}(\theta)}}{L_{p,0}}, \tag{2}$$

where $L_{p,0}$ is the phantom's original length and $\overrightarrow{L_{p,crd}}$ is the phantom's change in length which is a function of the implant bend angle $\overrightarrow{\theta}$.

$$\overrightarrow{\lambda} = 1 + \overrightarrow{\epsilon}, \tag{3}$$

where $\overrightarrow{\epsilon}$ is the strain.

From Eq. 1, it is necessary to optimize the trade-off between mechanical flexibility (θ) and the maximum tissue tension and elongation possible (F_{4x} and $L_{p,crd}(\theta)$). In the following subsection we model the flexible rack in order to quantify $L_{p,crd}(\theta)$ and the resultant F_{4x} as as a function of flexible rack parameters.

A. Flexible Rack Model - Beam Spring Behaviour

The rack is assumed to be a dynamic cantilever beam (i.e. a beam that changes length over time) with homogeneous and isotropic properties. The theory of bending moments (Euler-Bernoulli beam equation) is utilized to compute the maximum rack deflection at the free end (point M_0 in Fig. 4), the slope at the free end, and the maximum tissue elongation. The assumed cantilever beam is a dynamic system that increases in length with a varying slope over time. A simple approximation could be to assume that the $L_{p,crd}$ (tissue elongation length) is the arc length (S) minus the rack deflection at the free end γ_{max}

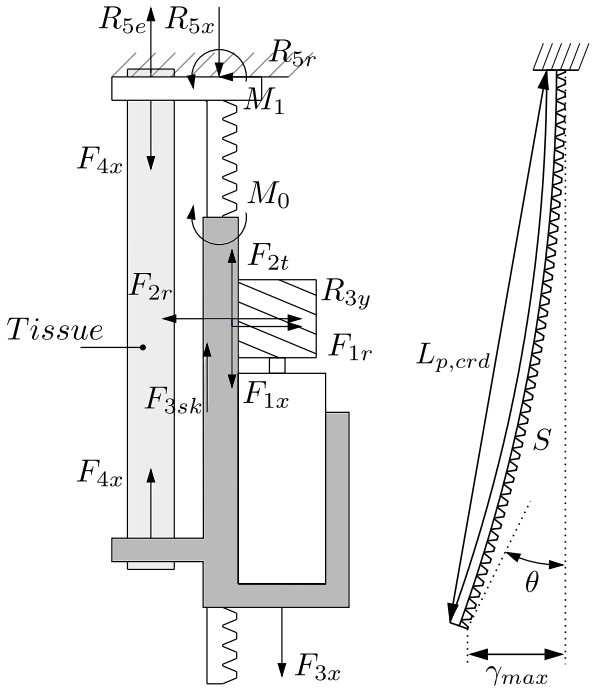

Fig. 4. A free body diagram of the FEIR model: (a) the forces on the DC gearmotor, right-hand worm screw, flexible rack, rigid fixed and rails, and the esophagus (side view schematic) and (b) the rack slope/implant bend angle (θ) and rack deflection (γ_{max}).

(Fig. 4). With those assumptions, the flexible rack is modelled by Eq. 4 and 5 to compute $L_{p,crd}$ and θ. Note that we denote the slope of the cantilever free end (θ) as the implant bend angle. The computed $L_{p,crd}$ and θ values are then used to approximate the tissue tension via the non-linear phantom model (Eq. 1).

The static analysis is solved iteratively where for each rack expansion step (pre-defined) the bending moment, implant bend angle, slope deflection, phantom elongation length, and phantom tension are computed. The initial values of the iterative solution are $\theta = L_{p,crd} = M_0 = \gamma = F_{4x} = S = 0.00$ (i.e. no rack expansion).

$$\overrightarrow{L_{p,crd}} = \overrightarrow{S} - \overrightarrow{\gamma_{max}}, \tag{4}$$

where S is the curvilinear abscissa of the rack and γ_{max} is the rack deflection at the free end.

$$\overrightarrow{\theta} = \frac{\overrightarrow{M_0}\odot\overrightarrow{S}}{E_r I_r}, \tag{5}$$

where E_r is the rack material Young's modulus, and I_r is the moment of inertia.

The maximum rack deflection (γ_{max}) and the bending moment (M_0) are given by Eq. 6 and Eq. 7, respectively.

$$\overrightarrow{\gamma_{max}} = \frac{\overrightarrow{M_0}\odot\overrightarrow{S}\odot\overrightarrow{S}}{2E_r I_r}, \tag{6}$$

$$\overrightarrow{M_0} = x\overrightarrow{f_{4x}}\odot\bigg(\sin\big(\arctan\left(18.00/27.50\right)\big) + \cos\big(\overrightarrow{\theta}\big)\bigg), \tag{7}$$

where x is the distance between the center of the attachment ring and the center of the rack base (in terms of thickness).

Assuming the rack is a rectangular beam, the area moment of inertia (I_r) is given in Eq. 8.

$$I_r = \frac{bh^3}{12.00}, \tag{8}$$

where b and h are the width and thickness of the rack base, respectively.

B. Structural Analysis of the Flexible Rack

We modelled the mechanical behavior of the rack using the finite element approach (FEM) on ANSYS to analyse its structural stability. The following assumptions were made when simulating the rack in ANSYS: (1) the rack material is isotropic, (2) the rack material is incompressible, (3) the simulation includes linear effects, and (4) the material is hyper-elastic and follows a neo-Hookean model. In this modelling, a 10 Node Tetrahedral Structural Solid was used. The simulation setup and results are shown in Subsection V-D.

C. Actuation Modelling

In this subsection we introduce an actuation model in order to determine the desired gearmotor torque (T) based on the FEIR maximum tension requirement (F_{4x}) and the worm screw and rack force components. The FEIR model mainly consists of a fixed support, a rigid rail, a flexible rack, and an esophagus, as shown in Fig. 4. The flexible rack and esophagus are attached to the fixed support from one end. The opposite end of the esophagus is attached to the rigid rail. The rigid rail slides across the fixed rack via the DC gearmotor to apply tension on the esophagus phantom.

In our model, the redundant rail is assumed to be a fixed support to which the flexible rack and esophagus are attached (Fig. 4). The rack–rail interface was empirically measured to have a dry static friction coefficient of 0.20 and was assumed to have a dry kinetic friction coefficient of 0.20. The worm screw–rack interface was assumed to have a dry static friction coefficient of 0.50 and a dry kinetic friction coefficient of 0.50. Friction between the tissue and implant encapsulation surfaces was ignored as it is relatively negligible. It was also assumed that the FEIR weight would be supported by the connective tissue that joins the surrounding organs.

The tangential force of the worm screw and the axial force of the rack, F_{1t}, F_{2x}, are given by Eq. 9. Assuming the worm screw and gearmotor are rigidly connected, the axial force of the worm screw and tangential force of the rack, F_{1x}, F_{2t}, are given by Eq. 10. The radial force components of the worm screw and rack, F_{1r}, F_{2r}, can be calculated as in Eq. 11.

$$F_{1t} = F_{2x} = \frac{2T}{d_1}. \tag{9}$$

$$F_{1x} = F_{2t} = \frac{2T}{d_1}\frac{\cos\alpha_n \cos\gamma - \mu_{sw}\sin\gamma}{\cos\alpha_n \sin\gamma + \mu_{sw}\cos\gamma}. \tag{10}$$

$$F_{1r} = F_{2r} = \frac{2T}{d_1}\frac{\sin\alpha_n}{\cos\alpha_n \sin\gamma + \mu_{sw}\cos\gamma}. \tag{11}$$

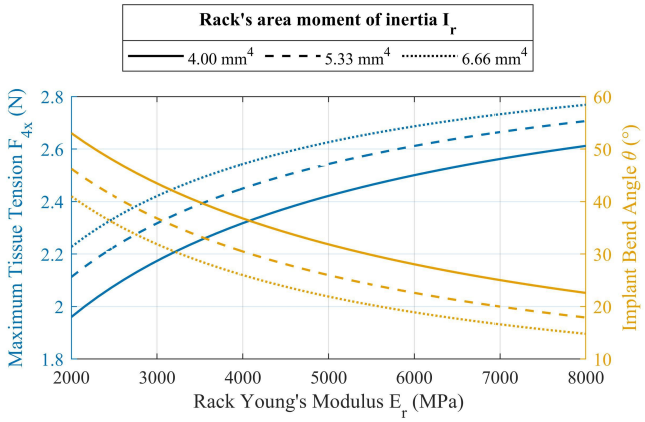

Fig. 5. Theoretical maximum tissue tension at $S = 100$ mm and corresponding implant bend angle as a function of rack flexibility.

The mechanical efficiency, η_r, of the worm and rack depends mainly on the gear-tooth lead angle and the coefficients of friction; it can be determined by Eq. 12:

$$\eta_r = \frac{\cos\alpha_n - \mu_{sw}\tan\gamma}{\cos\alpha_n + \mu_{sw}\cot\gamma}. \tag{12}$$

The tension in the esophagus, F_{4x}, can be calculated as follows:

$$F_{4x} = F_{3x} - F_{3sk}. \tag{13}$$

Assuming the gearmotor and rail are rigidly connected and that the rack does not bend, the axial force acting on the rail, F_{3x}, is equal to the axial force of the worm screw, F_{1x}, which is given by:

$$F_{3x} = F_{1x} = \frac{2T}{d_1}\frac{\cos\alpha_n \cos\gamma - \mu_{sw}\sin\gamma}{\cos\alpha_n \sin\gamma + \mu_{sw}\cos\gamma}. \tag{14}$$

The static friction force, F_{3sk}, between the rack and the rail is given by Eq. 15:

$$F_{3sk} = \mu_{sr} R_{3y}. \tag{15}$$

Substituting the tangential force component F_{1t} into Eq. 11 gives:

$$R_{3y} = \frac{2T}{d_1}\frac{\sin\alpha_n}{\cos\alpha_n \sin\gamma + \mu_{sw}\cos\gamma}. \tag{16}$$

Substituting the vertical reaction force of the rail on the rack, R_{3y}, into Eq. 15 gives the static friction force, F_{3sk}, as a function of the gearmotor torque, T, (Eq. 17).

$$F_{3sk} = \mu_{sr}\frac{2T}{d_1}\frac{\sin\alpha_n}{\cos\alpha_n \sin\gamma + \mu_{sw}\cos\gamma}. \tag{17}$$

The axial force acting on the rail (F_{3x}) and the friction between the rack and the rail (F_{3sk}) are then substituted into Eq. 13 to give the desired gearmotor output torque, T, as a function of the desired tension force and the gearset specifications (Eq. 18). A torque safety factor ($S_f = 2$) is added to Eq. 18 to account for unanticipated operating conditions.

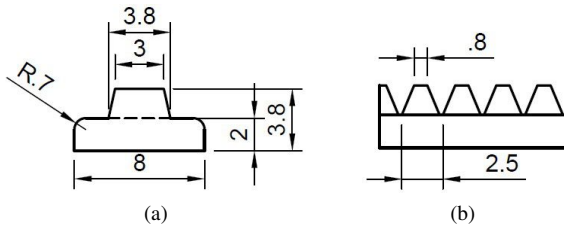

Fig. 6. Flexible rack dimensions in mm units; (a) front view and (b) side view.

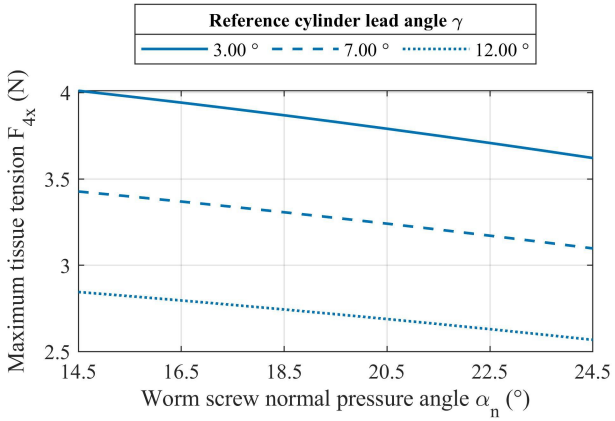

Fig. 7. Theoretical maximum tissue tension at $S = 100\,\text{mm}$ for different pressure and lead angles, for a worm screw diameter $d_1 = 13\,\text{mm}$ and maximum actuation torque $T = 16.1\,\text{Nmm}$ (assuming no rack bending).

$$T = \frac{S_f F_{4x} d_1}{2} \frac{\cos\alpha_n \sin\gamma + \mu_{sw}\cos\gamma}{\cos\alpha_n \cos\gamma - \mu_{sw}\sin\gamma - \mu_{sr}\sin\alpha_n}. \quad (18)$$

V. Theoretical Results

In this section, we present the theoretical results to assess the feasibility and performance of a flexible rack. There are two primary sets of design variables that dictate the implant performance (maximum tension force and tissue elongation length) with respect to the clinical requirements of the implant; (1) rack base area moment of inertia and Young's modulus and (2) rack and worm screw teeth geometries.

A. Rack base design

Figure 5 shows the model theoretical maximum tension force achieved by the implant and the corresponding implant bend angle as a function of the rack flexibility (Young's modulus) and area moment of inertia I_r (Eq. 1 and 5). As hypothesised, when the rack is more flexible (i.e. smaller E_r and I_r values) it bend bends more and results in a smaller tension force. We chose to use an $E_r = 3800\,\text{MPa}$ (3D printed Polylactide, PLA) and an $I_r = 5.33\,\text{mm}^4$ to achieve $F_{4x} \leq 2.40\,\text{N}$. Even though $F_{4x} = 2.00\,\text{N}$ is the requirement, $F_{4x} \leq 2.40\,\text{N}$ was chosen as a safety-factor. 3D printed PLA was chosen as it is a readily accessible material and is sufficient to demonstrate the contributions of the the theoretical framework developed and the flexible rack.

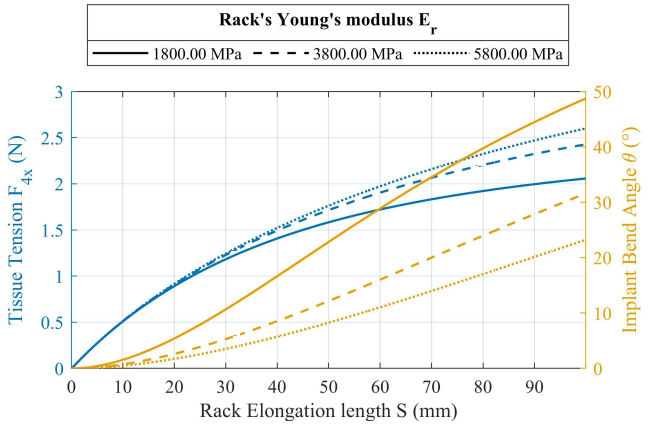

Fig. 8. Theoretical tissue tension and corresponding implant bend angle as a function of rack elongation length and Young's modulus.

TABLE I
Worm screw and rack force results.

Parameter	Notation	Value	Unit
Desired tension force in the esophagus	F_{4x}	2.00	N
Torque safety factor	S_f	2.00	-
Desired gearmotor torque	T	16.10	Nmm
Worm tangential force	F_{1t}	1.24	N
Worm axial force	F_{1x}	2.11	N
Worm radial force	F_{1r}	0.56	N
Rack tangential force	F_{2t}	2.11	N
Rack axial force	F_{2x}	1.24	N
Rack radial force	F_{2r}	0.56	N
Efficiency worm/rack	η_r	8.96	%

B. Rack and worm screw teeth geometry design

The rack and worm screw teeth geometries (d_1, γ, and α_n) along with the required tension force ($F_{4x} = 2.00\,\text{N}$) define the necessary actuation torque (Eq. 18). To achieve the implant's compact gear configuration (i.e. gear-meshing, Fig. 2), the worm screw diameter d_1 must be larger than the motor thickness, but not too large as it has an inverse relationship with the achievable force F_{4x}. Therefore, the diameter was chosen to be $d_1 = 13.00\,\text{mm}$.

The rack and worm screw teeth geometries were chosen ($\gamma = 3.00\,°$, and $\alpha_n = 14.50\,°$) based on practical standards to maximise the achievable tension force, reduce backlash, and achieve a self-locking actuation mechanism (Section IX-B of the Supplementary materials). The dimensions of the flexible rack are shown in Fig. 6.

Table I provides the results of the actuation model (Eq. 9 to 18) and concludes that a torque of $16.10\,\text{Nmm}$ (with a safety factor $S_f = 2.00$) is required to achieve $F_{4x} = 2.00\,\text{N}$ tissue tension force for the chosen rack and worm screw teeth geometries. Note that the typical worm screw geometry ranges are $\gamma = [3.00, 12.00]\,°$ and $\alpha_n = [14.25, 25.00]\,°$ and that increasing either parameters leads to a decrease in achievable tension force (for a fixed $d_1 = 13.00\,\text{mm}$ and $T = 16.10\,\text{Nmm}$ and assuming no rack bending Fig. 7). The actuation model result shown in Fig. 7 demonstrates that the

chosen gear geometries produce the largest maximum tissue tension $F_{4x} = 4.00\,\text{N}$.

C. Theoretical implant tension performance

Once the FEIR design variables (i.e. rack and worm screw design) are determined, the theoretical tissue tension and implant bend angle can be found at each incremental rack expansion length $S = [0, 100]\,\text{mm}$ via Eq. 1 and 5. Using a PLA rack ($E_r = 3800.00\,\text{MPa}$) with $I_r = 5.33\,\text{mm}^4$, $\gamma = 3.00\,°$, $\alpha_n = 14.50\,°$, and $d_1 = 13.00\,\text{mm}$ the theoretical tissue tension and implant bend angle are shown in Fig. 8. We also show how the tension and implant bend angle vary for if the Young's modulus value is varied but the geometrical variables are kept fixed (Fig. 8). The Figure demonstrates that initially at small elongation lengths the tissue tension increases at a steep rate relative to larger elongation lengths (Fig. 8). Contrarily, the implant bend angle increases gradually at small elongation lengths until it reaches an approximately constant rate of change at larger elongation lengths. The theoretical maximum tissue tension and implant bend angle at $S = 100.00\,\text{mm}$ for the PLA rack ($E_r = 3800.00\,\text{MPa}$) are $2.43\,\text{N}$ and $31.59\,°$. At the low Young's modulus value ($E_r = 1800.00\,\text{MPa}$) the implant bends significantly more and results in a significant tension drop. At the large Young's modulus value ($E_r = 5800.00\,\text{MPa}$) the implant is less flexible and only provides a marginal tension increase. Therefore, a Young's modulus in the range of $E_r = 3800.00\,\text{MPa}$ provides a trade-off between flexibility and the attainable tension tension.

D. Structural Analysis Results

We conducted tests for structural deformation and stress of the flexible PLA rack using the numerical model developed in ANSYS. We tested the rack with the conditions of a simply-supported beam, where a shearing load was applied at the middle of the rack $S = 50.00\,\text{mm}$, with both ends of the rack modelled as fixed (three-point bend test). We considered the off-track length of the rack to be the maximum at $S = 100.00\,\text{mm}$, where it is the least supported by the rails. The three point bend test and the shear force location and direction (on the rack base plane in the positive x-axis direction shown in Fig. 9) were chosen to model the rack bending direction that occurs due to the tissue tension and ring placement as the FEIR expands.

The shear force was set to $w = 5.00\,\text{N}$ as the maximum axial load on the rack to apply $2.00\,\text{N}$ of tissue tension was computed to be $2.11\,\text{N}$ for the FEIR model; the FEIR rack would thus experience $4.22\,\text{N}$ (double the worm axial force due to the presence of two worm screws in the FEIR, Table I). The ultimate tensile strength (UTS) and Young's modulus of the 3D printed PLA were set to $3800\,\text{MPa}$ and $53.00\,\text{MPa}$, respectively. The Poisson's ratio was assumed to be 0.36. The rack dimensions are provided in Subsection V-B and Fig. 6 of the supplementary materials. The simulation was subject to the boundary conditions in Eq. 19.

$$\begin{aligned} &w(0) = 0.00\,m, \quad w''(0) = 0.00\,Nm, \\ &w''(100.00) = 0.00\,Nm, \quad w'''(50.00) = 5.00\,N, \end{aligned} \tag{19}$$

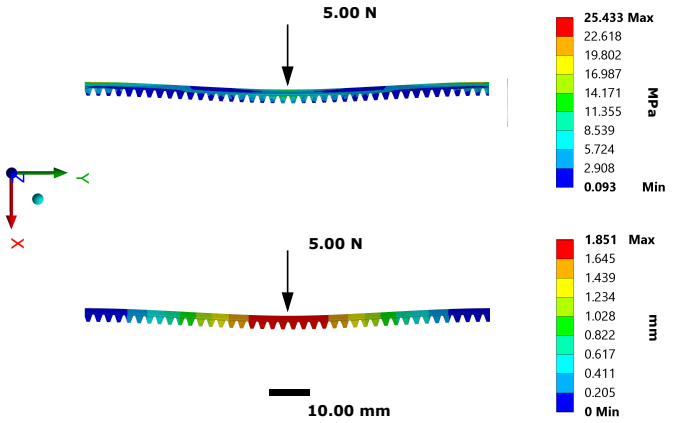

Fig. 9. Structural analysis results of applying $5.00\,\text{N}$ to the middle of the PLA rack; the top diagram shows the stress distribution and the bottom diagram shows the rack deformation.

where $w(0.00)$ is the rack deflection at the fixed end, $w''(0.00)$ is the the bending moment of the rack at $0.00\,\text{mm}$, $w''(100.00)$ is the the bending moment of the rack at $100.00\,\text{mm}$, and $w'''(50.00)$ is the shearing force on the rack at $50.00\,\text{mm}$.

The stress distribution and maximum deflection of the PLA rack are demonstrated in Fig. 9. The maximum stress and maximum deflection are $25.43\,\text{MPa}$ and $1.85\,\text{mm}$, respectively. Therefore, the maximum stress value $25.43\,\text{MPa}$ indicates that PLA is structurally stable material for the flexible implant as it has an UTS of $53.00\,\text{MPa}$.

VI. Experimental Results

In the following experiments we validate the implant's capability of achieving $2.00\,\text{N}$ of tissue tension and $100.00\,\text{mm}$ tissue elongation, as well demonstrate the benefits of using a flexible rack.

A. Experimental setup

During the experiment, the robotic implant was suspended in the air (unless otherwise stated). Data communication between the implant and a PC was via a serial communication interface. A graphical user interface (GUI) displayed the sensor readings in real-time and allowed force and displacement commands to be sent to the implant. The experiment was performed on an esophagus phantom made by casting Ecoflex 00-30 from Smooth-On Inc. (Section IX-C of the Supplementary materials). Data analysis was carried out in MATLAB, and a moving average filter was applied to the force and implant bend angle signals in Fig. 10, 11c, and 11d.

We used a permanent magnet brushed DC (PMDC) gearmotor (Kingly Gear Co., Ltd) with stall, rate-load, and maximum efficiency torques of 245.00, 29.00, and $21.80\,\text{Nmm}$, respectively. The PLA rack was 3D printed (Printer Original Prusa i3 MK3) with an infill solid density of $70.00\,\%$ and a layer height of $0.20\,\text{mm}$. The worm screw, rails, and hinges were 3D-printed using the Mojo Printer-Strastasys with an infill solid density of $100.00\,\%$ and a layer height of $0.127\,\text{mm}$.

A resistive flex sensor (FSL0095103ST, Spectra Symbol) was placed between the rack and the rails to measure the

implant bend angle (note that the stiffness of the resistive flex sensor is negligible and is therefore omitted from the mathematical model in Section IV-A). Raw data was collected from the sensor bent at different angles, and a sixth-order polynomial model was utilized to compute the angles. Using the flex sensor, the implant with the PLA rack was found to be capable of bending within the range of -35.00 to $35.00\,^{\circ}$.

B. Experimental implant tension performance

In this subsection, we experimentally determine the maximum tissue tension applied to the tissue via the FEIR using a PLA rack. In order to measure the maximum tissue tension, the two gearmotors were powered on in opposite directions, increasing the tissue length by $88.10\,$mm. The experiment was repeated three times and the mean $\pm$ standard deviation of the tissue tension and implant bend angle were computed. Note that zero point calibration was applied to the experimental implant bend angle curve shown in Fig. 10; the resting state bend angle ($2.03\,^{\circ}$) was subtracted from the implant bend angle values. The dead zone ($[0.00, 10.50]\,$mm) in the theoretical tissue tension values represent the slack in the tissue phantom when the implant was fully retracted. As shown in Fig. 10, the tissue tension and implant bend angle both increase overtime. The implant bend angle appears to reach a steady state value from $70.00\,$mm while the tissue tension value continues increasing until the maximum elongation length. This is hypothesised to be due to the difference between the force required to elongate the tissue phantom and the force required to bend the FEIR. After the FEIR expands by $70.00\,$mm at an approximate $20.00\,^{\circ}$ implant bend angle, the force required to bend the implant further ($> 20.00\,^{\circ}$) is more than the force required to expand the implant and elongate the tissue phantom further ($> 70.00\,$mm).

Note that as the implant expands to increase the tissue tension, it naturally bends inwards (positive bend angle). The implant achieved an average tissue tension $F_{4x} = 2.94\,$N at a bend angle $\theta = 21.73\,^{\circ}$, and therefore satisfied the implant design requirements. From Fig. 10, the experimental and theoretical tissue tension values are within reasonable agreement with a root-mean-square error (RMSE) of $0.26\,$N. However, the implant bend angle results have a RMSE of $4.97\,^{\circ}$. The mismatch between the theoretical and experimental implant bend angles is hypothesised to be due to the assumption that the rack's theoretical model is a rectangular beam with a homogeneous and isotropic Young's modulus as in Section IV-A, while the 3D printed rack is likely to have a smaller anisotropic and inhomogeneous Young's modulus. Additionally, the standard deviation values of the implant bend angle indicate inaccuracies of the resistive flex sensor.

C. Implant recovery from bending disturbance

Although flexible actuators are more prone to external disturbances, the force control developed (see Supplementary Material, Section IX-E) yields a flexible implant that actively copes with external disturbances. We determined that the bending of the FEIR could stem from two main sources; namely, the coupling between the soft tissue and the flexible

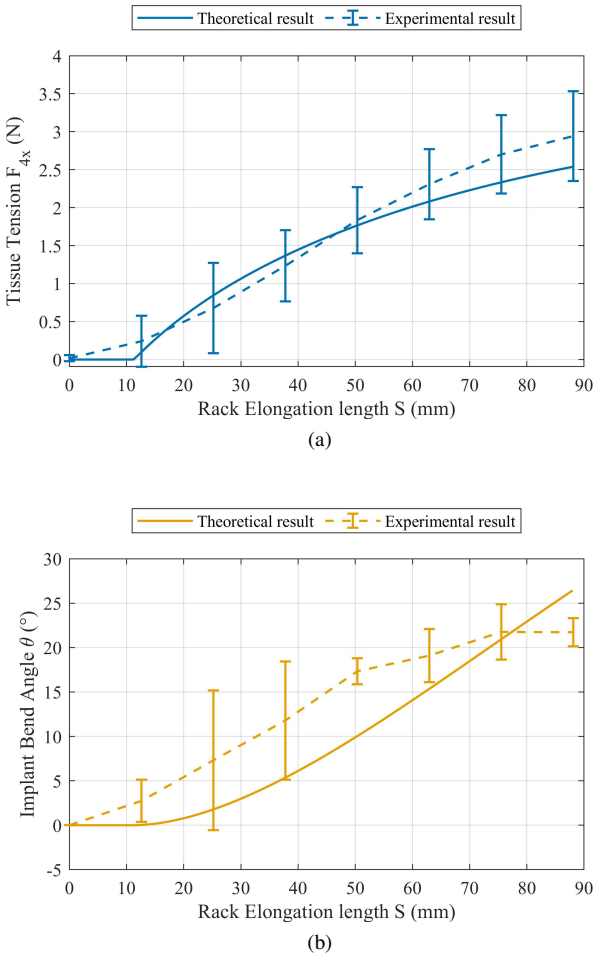

Fig. 10. Theoretical and experimental tissue tension (a) and corresponding implant bend angle (b) as a function of rack elongation length using a PLA rack. The experimental results are the mean and standard deviation of three experimental tests.

rack and the curving of the patient's torso while wearing the implant. Consequently, the flexible robotic implant can bend inwards (Fig. 11a) or outwards (Fig. 11b). In the case of an inward-disturbance, the force exerted on the esophagus is reduced; ideally, then, the implant should elongate further to compensate for the lost tissue tension. In the case of an outward disturbance, the force acting on the esophagus will increase, so the implant should retract to reduce the tissue tension. As the outward disturbance increases the tissue tension beyond the desired set-point, it poses the risk of tearing the tissue. Our previous studies have shown that swine esophageal tissue shows no obvious damage from application of forces as high as 4 N in bench top tests [16]. In this subsection we carry out a qualitative experiment using the PLA rack to verify the implant's disturbance rejection capability.

We performed two experiments: one on adult swine esophagus and one on a phantom esophagus (Ecoflex 00-30) to verify whether the PI controller could successfully reject disturbances. The swine esophagus was brought frozen from a slaughterhouse, after which it was placed in saline solution and stored in a refrigerator at $2.00\,^{\circ}$ C for $24.00\,$hours before being used. The two experiments involved setting the tissue

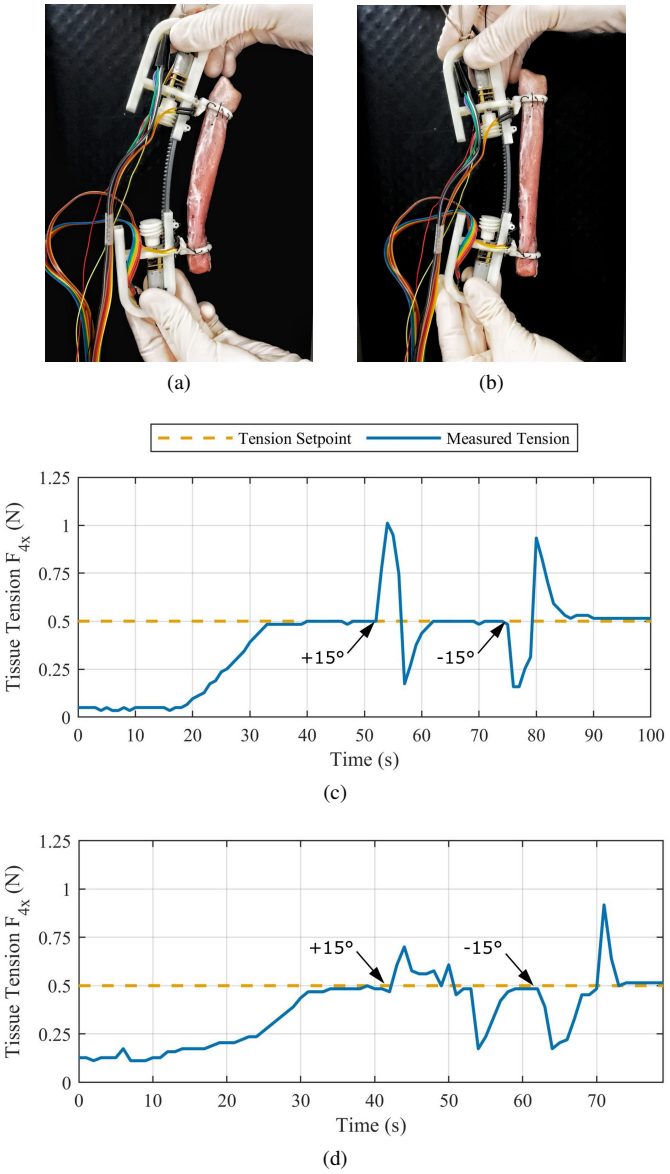

Fig. 11. Bending of the implant with an adult swine esophagus to simulate an external disturbance: (a) the robot is bent inwards $+15.00\,^{\circ}$ (decreasing tension); (b) the robot is bent outwards $-15.00\,^{\circ}$ (increasing tension); (c) the closed-loop force control results for the esophagus phantom; and (d) swine esophagus result.

tension to $0.50\,\mathrm{N}$, a set-point arbitrarily chosen within the 2 N range. Once the implant reached steady state, it was manually bent inward and outward, and the tissue tension set-point tracking performance was monitored, as seen in Fig. 11a). The implant's disturbance rejection performance is reported in Fig. 11c for the esophagus phantom and Fig. 11d for the swine esophagus. As shown in Fig. 11c, at 32.00 seconds, the robot reached the force set-point ($0.50\,\mathrm{N}$); at 52 seconds, the robot was bent outwards. Consequently, the tissue tension increased, and the implant successfully retracted to reduce the force back to set-point. When the robot was released at 57.00 seconds, the tissue tension became smaller than the set-point; accordingly, the implant expanded to increase the force. Furthermore, the implant was bent inwards at the 75.00^{th} second and released at the 80.00^{th} second, mirroring the behavior described above. The results in Fig. 11d demonstrate the same experiment and results on the swine esophagus.

This experiment has shown that the FEIR is capable of maintaining the desired tension force in the esophagus and associated tissue length in the presence of positive and negative disturbances. In Section IX-F of the Supplementary Material, we carry out a quantitative experiment to measure the implant's recovery time from disturbances.

D. Encapsulation fatigue life

As the implant dynamically changes its size, shape, the encapsulation experiences shear forces from the skeletal system, such as the ribs, when the implant resides in the chest cavity. In this subsection, we experimentally verify the effects of the rack flexibility on the fatigue life of an elastomeric sleeve proxy using a rack proxy. We tested the fatigue life of the miniature elastomeric sleeve with the two rack types (PLA and ABSplus), using the experimental setup and procedure described in Section IX-D of the Supplementary Material. We ran three experimental trials per rack type and measured the number of strokes required to break the elastomeric sleeve. The elastomeric sleeve broke after $5.07 \cdot 10^3 \pm 1.32 \cdot 10^3$ and $21.10 \cdot 10^3 \pm 1.37 \cdot 10^3$ strokes using the PLA and ABSplus racks, respectively. From the results, as the rack's flexibility increased, the fatigue life of the encapsulation sleeve was improved. It is hypothesised that the fatigue life improvement is due to a reduction in the shear force applied to the encapsulation sleeve (i.e. the more flexible the rack, the easier it deflects away from the force, the smaller the shear force).

The ABSplus rack, being more flexible, deflected the most under shear, and thus its encapsulation sleeve fatigue life was the longest. However, as the PLA rack is less flexible, the encapsulation sleeve was found to degrade and reach failure at a higher rate than ABSplus. Overall, this result suggests that a flexible implant increases the protective sleeve fatigue life. The ABSplus material was not chosen for the rack as it would require the rack base to be larger in order to achieve the same tension force provided by the PLA rack.

E. Implant-to-tissue contact force versus rack flexibility

An effective implant would minimise its pressure on surrounding tissue to reduce inflammation. To quantify the effect of the rack flexibility on the contact force between the implant and surrounding tissue, the experimental setup shown in Fig. 12 was developed. Two foam blocks (surrounding-tissue phantoms) were placed at the sides of the implant; each was fixed via two elastic bands. The top and bottom of the implant were covered with acrylic sheets. A nylon threaded rod (M8) with a rectangular acrylic face was utilized to deflect the implant center by up to $30.00\,\mathrm{mm}$ in $0.625\,\mathrm{mm}$ increments from the esophagus phantom side. The implant-to-tissue contact force was tested at $44.00\,\mathrm{mm}$ and $80.00\,\mathrm{mm}$ rack extension (Fig. 12) using the flexible PLA rack. Additionally, for a rigid implant benchmark, a $2.00\,\mathrm{mm}$ steel bar was tested at $80.00\,\mathrm{mm}$ extension in place of the rack. Finally, force-sensing resistors (FSRs) were placed between the implant rails

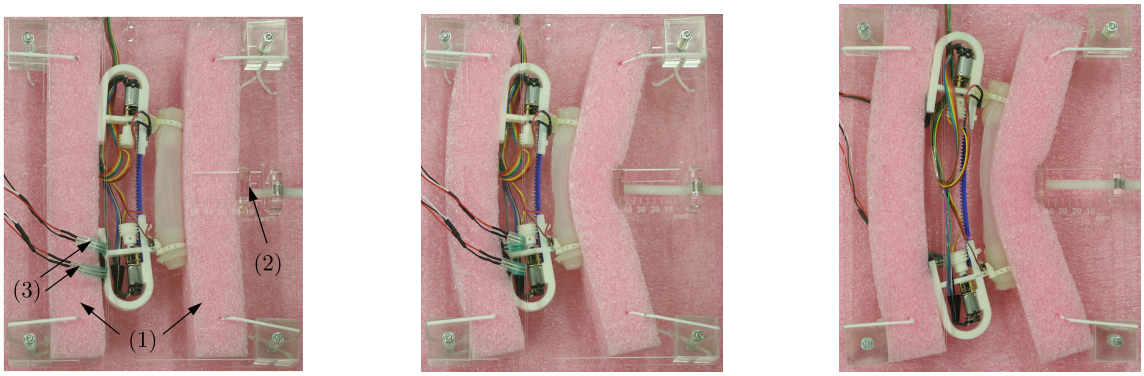

(a) (b) (c)

Fig. 12. Experimental setup to quantify the effect of rack flexibility on the contact forces between implant and surrounding tissue at varying deflections via a foam tissue phantom and force sensing resistors. (a) initial state using the PLA rack at 44.00 mm expansion. (1) shows the surrounding-tissue phantom, (2) is the rotary-based deflection mechanism, and (3) shows the force-sensing resistors. (b) final state using the PLA rack at 44.00 mm expansion and 30.00 mm implant deflection. (c) final state using the PLA rack at 80.00 mm expansion and 30.00 mm implant deflection.

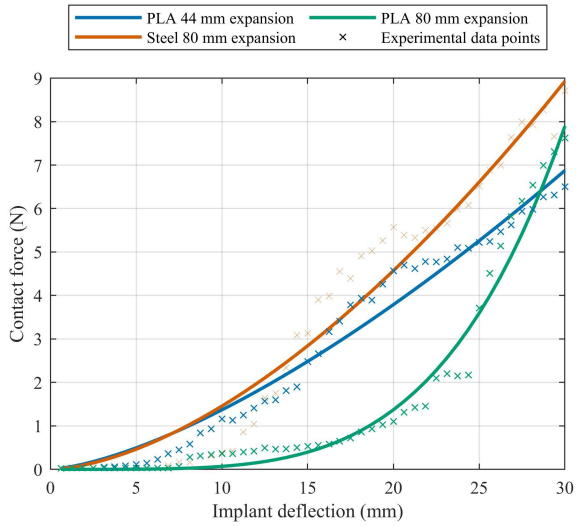

Fig. 13. Experimental contact force between implant and surrounding-tissue phantom as a function of the implant deflection for the ABSplus and PLA racks. Cross marks represent data points, and solid lines are fitted exponential lines to the data points.

and the surrounding-tissue phantoms to measure the contact force at each implant deflection increment. The results of this experiment are presented in Fig. 13. One-term power series models were fitted to each data set, as shown in the figure. As hypothesised, the rigid implant (steel 80.00 mm) yielded larger contact forces than the flexible implant (PLA 44.00 and 80.00 mm), as shown in Fig. 13. Consequently, a flexible implant would inflict less harm to the surrounding organs and minimize the undesirable fibrotic response.

For the flexible rack, the 80.00 mm implant expansion length resulted in a smaller implant-to-tissue phantom contact force compared to the 44.00 mm expansion length. The decrease in the implant-to-tissue phantom contact force is attributed to the fact that as an implant expands, the implant as a whole becomes more flexible. However, at high implant deflection values, the flexible rack at 80.00 mm expansion resulted in larger contact forces compared to 44.00 mm expansion. This is due to the fact that at 80.00 mm expansion, the implant is more flexible and bends significantly resulting in a smaller contact surface area between the implant rails and the surrounding tissue phantom (Fig. 12c on the left side). The smaller contact surface area leads to a higher contact force registered by the localized force sensor.

The change in the contact surface area indicates that for excessively flexible racks the implant would bend significantly and is likely to show a localized implant-to-tissue contact force peak. Therefore, when designing a flexible implant with rigid parts, the flexible element (i.e. rack Young's modulus and area moment of inertia) must be designed based on a trade-off between the implant's flexibility and its capability of maintaining a desired and safe shape. A more accurate tissue phantom and an array of sensors would give more insight into the contact force distribution.

VII. Discussion

We investigated the properties of the flexible rack via the theoretical and numerical models and showed how the rack material and geometrical parameters affect its flexibility, rack stress, implant bending, and tissue tension. By utilising a rack with a Young's modulus of 3800.00 MPa and an area moment of inertia of 5.33 mm^4 and an actuation rate-load torque of $\leq$ 29.00 Nmm, the flexible implant was experimentally validated to bend up to $\pm 35.00\,^{\circ}$, elongate tissue by 100.00 mm, and apply up to 2.94 N tension force, thus satisfying the clinical requirements for LGEA.

While the literature provides no measurement of the contact forces between the stiff implant and the surrounding biological tissue, there is increasing evidence that mechanically compliant devices reduce these forces [4], [6]. Accordingly, we incrementally improved the stiff implant design from [17] via one-directional mechanical compliance (in the XY plane in Fig. 9) using a flexible rack. We experimentally validated in Section VI-E that the one-directional compliance of the rack reduces the 2D forces on surrounding tissue. In vivo, the implant will be fixed on the tissue in order for the compliant

face of the rack to bend with the spine. The actual validation of the effect of the flexible robot on tissues and measurement of robot-tissue interface forces will be carried out in vivo as future work. Although our group is currently investigating a completely soft robotic implant [20], the flexible implant is closer to clinical translation. While we envisage that the current FEIR can be implanted in eight-year old patients [16], miniaturisation will broaden the application of the device. The design of the FEIR inherited the overall tissue attachment features from our previous robotic implant [17] and thus the in vivo device implantation and extraction will be carried out in the same way.

Future work includes the exploration of durable gear and rack (yet flexible) materials and device miniaturisation. We have chosen PLA to demonstrate the modelling framework and the benefits of implant flexibility, but in a clinical setting it will be necessary to miniaturise the device and analyse material properties such as bending-strength, mesh stiffness, elastic modulus, coefficient of thermal expansion, and friction characteristics.

The theoretical framework proposed in this work enables the design and simulation of the FEIR with miniaturisation (smaller I_r), flexibility (smaller I_r and E_r), tissue tension force ($F_{4x} \geq 2.00\,\mathrm{N}$), and gear material properties requirements. For example, if the rack was to be machined from the more durable Polyamide 66 ($E_r = 3100\,\mathrm{MPa}$) then an $I_r = 6.15\,\mathrm{mm}^4$ would be necessary to achieve $F_{4x} \leq 2.40\,\mathrm{N}$. For Polyacetal-Copolymer ($E_r = 2600\,\mathrm{MPa}$) an $I_r = 7.33\,\mathrm{mm}^4$ would be required. In terms of miniaturisation, a smaller actuator with less torque can be utilised and the flexible rack and actuation models can be utilised to find the suitable rack material and teeth geometry. The theoretical model of the flexible rack in Section IV-A makes a simple approximation about the tissue elongation length which can be improved via continuum mechanics.

VIII. Conclusion

We introduced a flexible and expandable implantable robot along with a theoretical, numerical, and experimental framework for the design, mechanics optimization, and analysis of the FEIR to meet the essential clinical requirements of tissue health and ability of therapeutic treatments, defining the next generation of healthcare technology.

We have shown that by using a flexible rack, the implant can flex to accommodate external disturbances from body dynamics, reduce the implant-to-surrounding-tissue contact force, elongate the encapsulation sleeve fatigue life, and actively control the tissue tension in the presence of tension deviations. The mechanical compliance and active recovery from bending disturbance are essential features to accommodate volume changes inside the body and body postures and subsequently reduce the body's inflammatory response and avoid tissue damage. The implant's flexibility reduces the encapsulation's deterioration rate from mechanical wear. The mathematical models proposed are widely applicable and provide a flexible theoretical framework to select the best design parameters suited to an application. In the LGEA treatment, the theoretical framework can be applied towards clinical-grade FEIR design in terms of miniaturisation and implant material properties.

Acknowledgment

The authors thank Théo Lesignor, Dr. Shuhei Miyashita, XiaoFan Wu, Lilyan LeBlanc, Sarunas Nejus, and Eduardo Perez-Guagnelli for their input and assistance.

References

[1] S. Eming *et al.*, "Inflammation and metabolism in tissue repair and regeneration," *Science*, vol. 356, pp. 1026–1030, 2017.

[2] J. E. Foker *et al.*, "Development of a true primary repair for the full spectrum of esophageal atresia." *Annals of surgery*, vol. 226, no. 4, pp. 533–41; discussion 541–3, oct 1997.

[3] C. Angeli and A. Chatzinikolaou, "On-line fault detection techniques for technical systems: A survey." *IJCSA*, vol. 1, no. 1, pp. 12–30, 2004.

[4] P. Moshayedi *et al.*, "The relationship between glial cell mechanosensitivity and foreign body reactions in the central nervous system." *Biomaterials*, vol. 35, no. 13, pp. 3919–25, 2014.

[5] K. C. Spencer *et al.*, "Characterization of mechanically matched hydrogel coatings to improve the biocompatibility of neural implants," *Scientific reports*, vol. 7, no. 1, p. 1952, 2017.

[6] A. Carnicer-Lombarte *et al.*, "Mechanical matching of implant to host minimises foreign body reaction," *bioRxiv*, vol. 829648, 2020.

[7] W. A. Gray *et al.*, "S.M.A.R.T. self-expanding nitinol stent for the treatment of atherosclerotic lesions in the superficial femoral artery (STROLL): 1-year outcomes," *Journal of Vascular and Interventional Radiology*, vol. 26, no. 1, pp. 21–28, 2015.

[8] L. Xu *et al.*, "3D multifunctional integumentary membranes for spatiotemporal cardiac measurements and stimulation across the entire epicardium." *Nature communications*, vol. 5, p. 3329, 2014.

[9] E. T. Roche *et al.*, "Soft robotic sleeve supports heart function." *Science Translational Medicine*, vol. 9, no. 373, pp. 1–12, 2017.

[10] S. Miyashita *et al.*, "Ingestible, controllable, and degradable origami robot for patching stomach wounds," *Proceedings - IEEE International Conference on Robotics and Automation*, vol. 2016-June, no. 4, pp. 909–916, 2016.

[11] C. Huang *et al.*, "Mechanotherapy: Revisiting physical therapy and recruiting mechanobiology for a new era in medicine," *Trends in Molecular Medicine*, vol. 19, no. 9, pp. 555–564, 2013.

[12] K. Vining and D. J. Mooney, "Mechanical forces direct stem cell behaviour in development and regeneration." *Nature Reviews Molecular Cell Biology*, vol. 18, p. 728–742, 2017.

[13] A. Sutton *et al.*, "Photothermally triggered actuation of hybrid materials as a new platform for in vitro cell manipulation," *Nature Communications*, vol. 8, p. 14700, 2017.

[14] F. Sailhan, "Bone lengthening (distraction osteogenesis): a literature review," *Osteoporosis international*, vol. 22, no. 6, 2011.

[15] C. A. Cezar *et al.*, "Biologic-free mechanically induced muscle regeneration." *Proceedings of the National Academy of Sciences of the United States of America*, vol. 113, no. 6, pp. 1534–9, 2016.

[16] D. D. Damian *et al.*, "Design of a Robotic Implant for in-vivo Esophageal Tissue Growth," *Proceedings - IEEE International Conference on Robotics and Automation*, no. 1, pp. 73–74, 2014.

[17] ——, "In vivo tissue regeneration with robotic implants." *Science Robotics*, vol. 3, no. 14, p. eaaq0018, 2018.

[18] S. Al-Shanafey and J. Harvey, "Long gap esophageal atresia: an australian experience," *Journal of pediatric surgery*, vol. 43, no. 4, pp. 597–601, 2008.

[19] J. E. Foker *et al.*, "Long-gap esophageal atresia treated by growth induction: the biological potential and early follow-up results," in *Seminars in pediatric surgery*, vol. 18, no. 1. Elsevier, 2009, pp. 23–29.

[20] E. Perez-Guagnelli *et al.*, "Characterization, simulation and control of a soft helical pneumatic implantable robot for tissue regeneration," *IEEE Transactions on Medical Robotics and Bionics*, vol. 2, no. 1, pp. 94–103, 2020.

[21] S. P. Radzevich and D. W. Dudley, *Handbook of practical gear design*. CRC press, 1994.

IX. Supplementary Material

A. FEIR Electrical Design

A Baby Orangutan (Pololu) microcontroller was selected for this specific application because it provides two separate high-power motor drivers and is relatively small in size. Honeywell FSS1500NSR sensors were used to measure the force exerted against the tissue. These sensors provide low-amplitude signals that are conditioned by AD623 instrumentation amplifiers (Analog Devices), delivering a voltage gain of 22.00. The relative position of the implant was tracked using Pololu magnetic encoders to count the revolutions of the 298:1 DC motors. Because a power outage or any related disturbances would have undesired effects on this application, power redundancy is needed. Therefore, the system is designed so that it can be powered by either a 9.00-9.60 V battery pack or an external, plug-in power supply. The electrical design includes interfaces for both types of power supply to be connected simultaneously. It automatically switches to the power source that is characterized by a higher voltage, which, under normal operation, is the 12.00 V external power supply. If there is a power outage, the FEIR automatically starts receiving power from the battery. Fig. 14 illustrates the electrical topology on which the system is based.

Additionally, this concept enables the implant to be operated in an environment where electrical power from the grid is unavailable. A low-battery indicator is provided on the PCB to ensure that the operator is aware of it. Fig. 15 shows the PCB that has been designed for the FEIR, outlining the electrical interfaces.

B. Worm Screw Design

A normal pressure angle of 14.5 ° was chosen to limit the effects of center-distance changes (due to the rack flexibility) on backlash and for smoother running [21]. From Eq. 18, it can be seen that a decrease in the reference diameter and the lead angle results in a decrease in the required motor torque. Generally, to eliminate reverse driving and achieve self-locking, the lead angle must be below 6.00 ° [21]. However, as the lead angle decreases, it becomes more challenging to readily produce the worm screw. In this application, a self-locking mechanism is desirable to eliminate the need to continuously drive the worm screw to maintain tissue tension. Therefore, a lead angle of 3.00 ° was chosen. Finally, to produce the gear configuration shown in Fig. 4, the worm screw reference diameter was set at 13.00 mm. The worm screw specifications are listed in Section IX-B of the Supplementary Material. The dimensions of the worm screw are shown in Fig. 6.

C. Esophagus Phantom

The esophagus phantom (Ecoflex-30) utilized in this study was fabricated to have a tubular hollow shape and is characterized in Table II.

D. Experimental rig for testing the FEIR encapsulation's fatigue life

We developed an experimental test rig to simulate shear stress on the encapsulation sleeve (Fig 16). A diagram of the experimental setup is provided in the Supplementary Material. A servomotor rotates the arm/tip, causing the tip (a triangular prism with rounded corners) on the arm to stroke the elastomeric sleeve fixed on bars made from the three materials analyzed for the rack: PLA, Shell Shock, and ABSplus. We chose to apply a stroke frequency of 0.33 Hz, which was equal to a continuous arm rotation with a 5.00 ° central angle.

The experimental test rig utilized to simulate shear stress on the encapsulation sleeve in Section VI-D.

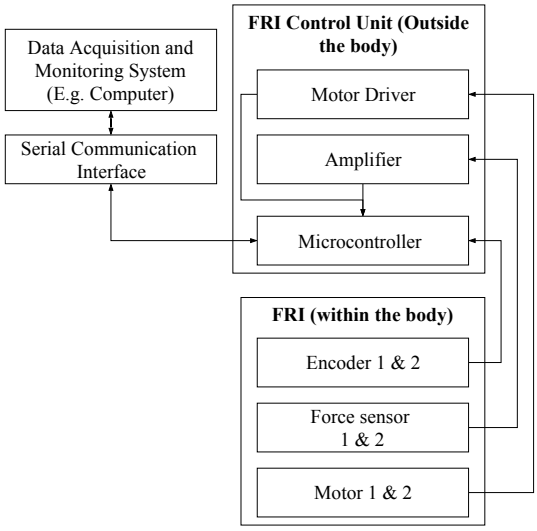

Fig. 14. Flexible Robotic Implant electrical topology within and outside the body.

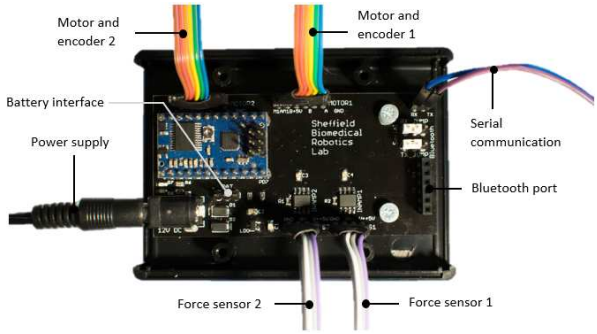

Fig. 15. Electronic circuit PCB

TABLE II
Esophagus phantom specifications.

Parameter		Value	Unit
Inner diameter		16.50	mm
Wall thickness		2.60	mm
Initial length	(L_0)	65.00	mm
Cross-sectional area	(A_p)	151.90	mm^2
Young's modulus	(E_p)	29.50	kPa

E. Control of the flexible robotic implant

The control goal is to control the PWM voltage input of the gearmotor in order to maintain the desired tension force in the esophagus in the presence of output disturbances and

TABLE III
FEIR WORM SCREW SPECIFICATIONS.

Parameter		Value	Unit
Tip diameter		14.50	mm
Reference diameter	d_1	13.00	mm
Number of teeth	z_1	1.00	-
Worm axial pitch / rack linear pitch	p_x	2.10	mm
Axial module	m_x	0.80	mm
Normal pressure angle	α_n	14.50	°
Reference cylinder lead angle	γ	3.00	°

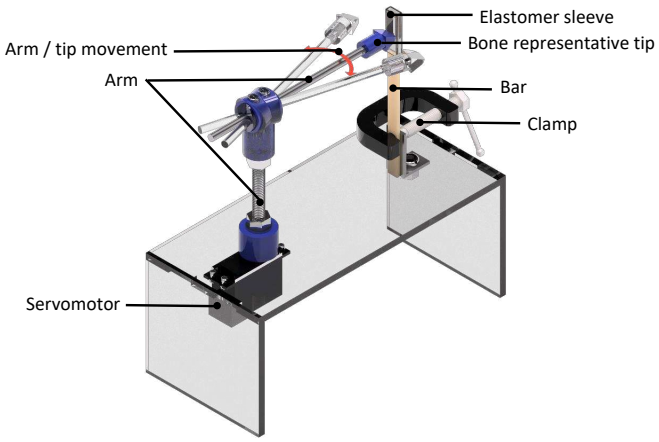

Fig. 16. Schematic of the experimental setup to investigate the effects of rack flexibility on the fatigue life of an elastomeric sleeve via the application of a stress versus number of cycles to failure test.

measurement noise. The variable to be controlled is the tension force applied to the tissue. The open-loop transfer function of the FEIR, whose tissue tension force output is a function of voltage input, is shown in Eq. 20:

$$\frac{Z(s)}{U(s)} = \frac{1}{s}\frac{4.443 \cdot 10^{-05}}{1.425 \cdot 10^{-07}s + 5.65 \cdot 10^{-06}}, \tag{20}$$

where $U(s)$ is the gearmotor voltage input in v and $Y(s)$ is the tissue tension in N. The transfer function of the FEIR was derived based on a viscous friction model of the gearmotor and on Newton's second law and Kirchhoff's voltage law. Note that there is parameter uncertainty in the underlying differential equations and therefore in the transfer function of the FEIR. Table IV lists the time-domain control requirements found to be relevant for tissue growth and integrity dynamics [17].

TABLE IV
FLEXIBLE ROBOTIC IMPLANT CONTROL PERFORMANCE COMPARISON.

Parameter	Desired	Achieved Unity gain P control	Achieved PI control	Unit
Target force	2.00	-	-	N
Overshoot	5.00	77.62	1.56	%
Rise time (5.00 − 95.00%)	5.00	1.98	3.00	s
Settling time (2.00%)	10.00	30.28	4.21	s
Steady-state error	0.00	0.00	0.00	N

TABLE V
FLEXIBLE ROBOTIC IMPLANT SYSTEM CONSTRAINTS.

Parameter	Minimum	Maximum	Unit
Gearmotor voltage	−6.00	6.00	V
Gearmotor speed	−75.00	75.00	RPM
Gearmotor acceleration	−31.00	31.00	RPM^2
Implant elongation	0.00	100.00	mm

1) System characteristics and analysis: This subsection will define the system constraints, measurement noise, and system disturbances, in order to model and control the FEIR system. The FEIR gearmotor has absolute and rate constraints on its output, which represent the minimum and maximum rotation speed and the falling and rising rates of the rotation speed (acceleration). The gearmotor also has an input absolute constraint that represents the minimum and maximum input voltage. Additionally, the FEIR has an absolute constraint on the minimum and maximum possible elongation, based on rack length. Table V provides the FEIR system constraint values.

The force sensors used to measure the tissue tension were assumed to have a normally distributed measurement noise of $\pm 5.00\,\%$ of the maximum tissue tension value, 2.00 N. The tissue tension force can be affected via external factors (disturbances), and it was assumed that any disturbance was constrained to $\pm 25.00\,\%$ of the maximum tissue tension value. Furthermore, there is parameter uncertainty in the FEIR system due to uncertainty in the gearmotor specifications and the tissue dynamics. Accordingly, the controller design methodology must account for input and output constraints, measurement noise, output disturbances, and parameter uncertainty. The FEIR system was modelled in Simulink; an overview of the model is provided in Fig. 17.

The system is linear time-invariant and has a single-input–single-output (SISO), second-order type 1 transfer function (Eq. 20). The system is open-loop unstable due to the integrator (the pole on the imaginary axis, Eq. 20). However, the closed-loop transfer function has two distinct real poles in the left half of the s-plane at -10.81 and -28.83. According to the Routh stability criterion, the system is closed-loop stable.

2) Controller design and simulation: The FEIR closed-loop response without a controller was simulated using Eq. 20 and a 2.00 N step input (without output disturbances and measurement noise). The step response characteristics are shown in Table IV. The step response (Table IV) demonstrates that, in order to meet the control requirements, the settling time and overshoot must be reduced. One possible control method to achieve this is the classical linear PID control law. However, the derivative term was omitted as derivative action introduces an increase into the controller's noise sensitivity. The proportional and integral gains were chosen via trial-and-error simulations on MATLAB and Simulink. The PI controller is given in Eq. 21. The step response characteristics of the system with the PI controller (without output disturbances and measurement noise) satisfy the control requirements, as shown in Table IV.

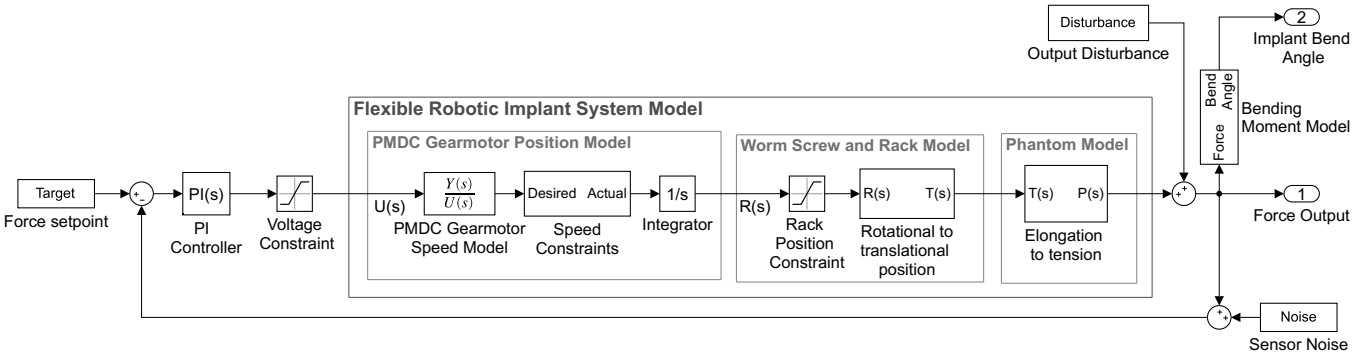

Fig. 17. Flexible robotic implant system closed-loop force control diagram demonstrating the gearmotor, gears, and esophagus phantom models. Where $U(s)$ is the input voltage in v, $R(s)$ is the rotational position output in radians, $T(s)$ is the transnational position output in mm, and $P(s)$ is the esophagus phantom tension in N.

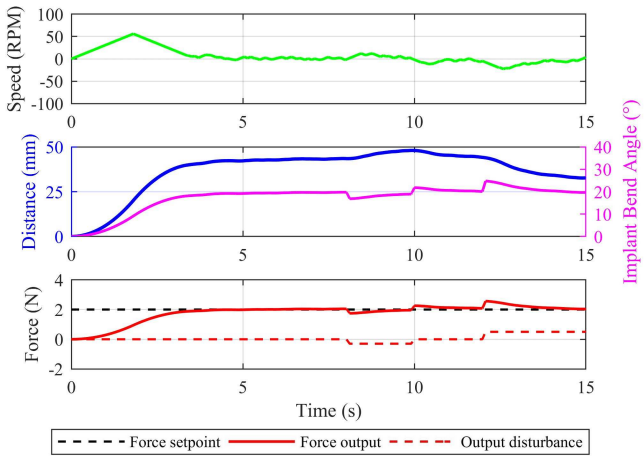

Fig. 18. Closed-loop force control simulation targeting 2.00 N, demonstrating disturbance rejection and robustness to sensor noise.

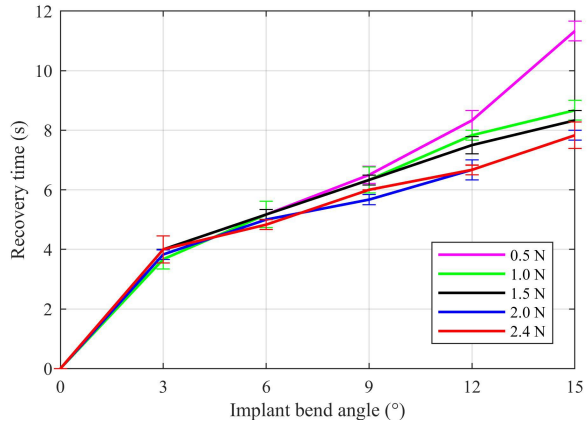

Fig. 19. Quantitative disturbance rejection performance when different forces are applied, using a PLA rack.

$$U(s) = 0.12 + \frac{0.001}{s}, \tag{21}$$

where $U(s)$ is the controller output.

The FEIR system with the PI controller was simulated using normally distrusted measurement noise ($\pm 5.00\,\%$) and output disturbances measuring -0.30 at seconds 8.00 to 10.00 and 0.50 at seconds 12.00 to 15.00. As can be seen in Fig. 18, the FEIR actuation was gradual and not abrupt, reducing the actuation load. Furthermore, the output disturbances, measurement noise, and input and output constraints demonstrated the controller's robustness.

To eliminate the mismatch in simulation and hardware-in-the-loop (HIL) results (due to modelling parameter uncertainty), the PI controller gains were fine-tuned through HIL tests.

F. Implant recovery time from disturbance

In this section, we discuss the recovery time of a flexed implant depending on the bending angle. We experimentally measured the implant recovery time depending on a bending disturbance. The experiment involved setting the tissue tension set-point, waiting for the implant to reach that set-point, and finally manually bending and holding (i.e., introducing a disturbance to) the implant to a defined angle. We defined the implant recovery time as the time it takes the implant to return to the set-point tissue tension from the moment the disturbance is applied.

We carried out this experiment via an experimental setup that included a platform with angles engraved on it, in the range of -15.00 to 15.00 in $3.00\,^\circ$ increments. The main rail of the FEIR was clamped, while the mirror rail was left mobile to be manually bent. We decided to apply an outward disturbance, because that poses the risk of tearing the tissue. The experiment was performed three times per angle across a range of tissue tension set-points.

As shown in Fig. 19, as the implant bend angle (disturbance) increased, the implant recovery time increased. This was expected, since an increase in disturbance results in a larger deviation from the force set-point; therefore, the implant must retract further, which takes a longer period of time. On the other hand, an increase in the set-point decreases the recovery time required when the disturbance is larger than $6.00\,^\circ$. This result may be explained by the fact that the control tracking error at larger set-points is more significant, so the controller reacts more aggressively.